scientific reports

OPEN

Characterization of mitochondrial health from human peripheral blood mononuclear cells to cerebral organoids derived from induced pluripotent stem cells

Angela Duong[1,2], Alesya Evstratova[1], Adam Sivitilli[3], J. Javier Hernandez[4,5], Jessica Gosio[4,5], Azizia Wahedi[6], Neal Sondheimer[4,6], Jeff L. Wrana[4,5], Jean-Martin Beaulieu[1✉], Liliana Attisano[3,7✉] & Ana C. Andreazza[1,2,8✉]

Mitochondrial health plays a crucial role in human brain development and diseases. However, the evaluation of mitochondrial health in the brain is not incorporated into clinical practice due to ethical and logistical concerns. As a result, the development of targeted mitochondrial therapeutics remains a significant challenge due to the lack of appropriate patient-derived brain tissues. To address these unmet needs, we developed cerebral organoids (COs) from induced pluripotent stem cells (iPSCs) derived from human peripheral blood mononuclear cells (PBMCs) and monitored mitochondrial health from the primary, reprogrammed and differentiated stages. Our results show preserved mitochondrial genetics, function and treatment responses across PBMCs to iPSCs to COs, and measurable neuronal activity in the COs. We expect our approach will serve as a model for more widespread evaluation of mitochondrial health relevant to a wide range of human diseases using readily accessible patient peripheral (PBMCs) and stem-cell derived brain tissue samples.

Mitochondrial dysfunction plays a crucial role in a wide range of human diseases[1,2]. The impact of aberrant mitochondrial activity is vast and disease burden will continue to increase unless we uncover their etiology and identify precise mitochondrial targets appropriate for the development of effective treatments. The brain consumes 20% of the total energy budget to power neuronal activity[3–5]. As a result, chronic mitochondrial dysfunction can have profound effects on neurotransmission and contributes to unwanted changes in neuronal circuits that underlie cognition, memory and other forms of neuronal plasticity[3,6,7]. The translation of this knowledge towards the development of effective drugs that target brain mitochondrial dysfunction remains at an early stage. This stagnation reflects a lack of adequate, functional, patient-derived models to study mitochondrial health and neuronal activity simultaneously. To date, tools for studying mitochondrial dysfunction have largely relied on postmortem brain samples, animal models or two-dimensional neuronal systems[8,9]. While these tools have been beneficial, they do not translate well into clinical applications, largely due to the lack of complex functions and neural circuits. These limitations restrict the accurate prediction of patient responses and screening of mitochondrial therapeutic compounds. In the absence of properly developed, patient-derived brain models capable of interrogating mitochondrial health, substantial barriers in testing etiological hypotheses and developing targeted mitochondrial therapeutics will continue to persist.

Cerebral organoids (CO) have become an essential tool for evaluating human brain development and diseases[10]. The ability of CO to differentiate into many cell types and self-organize three-dimensionally makes

[1]Department of Pharmacology and Toxicology, University of Toronto, Toronto, ON M5S 1A8, Canada. [2]Centre for Addiction and Mental Health, Toronto, ON M5T 1R8, Canada. [3]Department of Biochemistry, University of Toronto, Toronto, ON M5S 1A8, Canada. [4]Department of Molecular Genetics, University of Toronto, Toronto, ON M5S 1A8, Canada. [5]Lunenfeld-Tanenbaum Research Institute, Toronto, ON M5G 1X5, Canada. [6]Program in Genetics and Genome Biology, Peter Gilgan Centre for Research and Learning, The Hospital for Sick Children, Toronto, ON M5G 0A4, Canada. [7]Donnelly Centre for Cellular and Biomolecular Research, University of Toronto, Toronto, ON M5S 3E1, Canada. [8]Department of Psychiatry, University of Toronto, Toronto, ON M5S 1A8, Canada. ✉email: martin.beaulieu@utoronto.ca; liliana.attisano@utoronto.ca; ana.andreazza@utoronto.ca
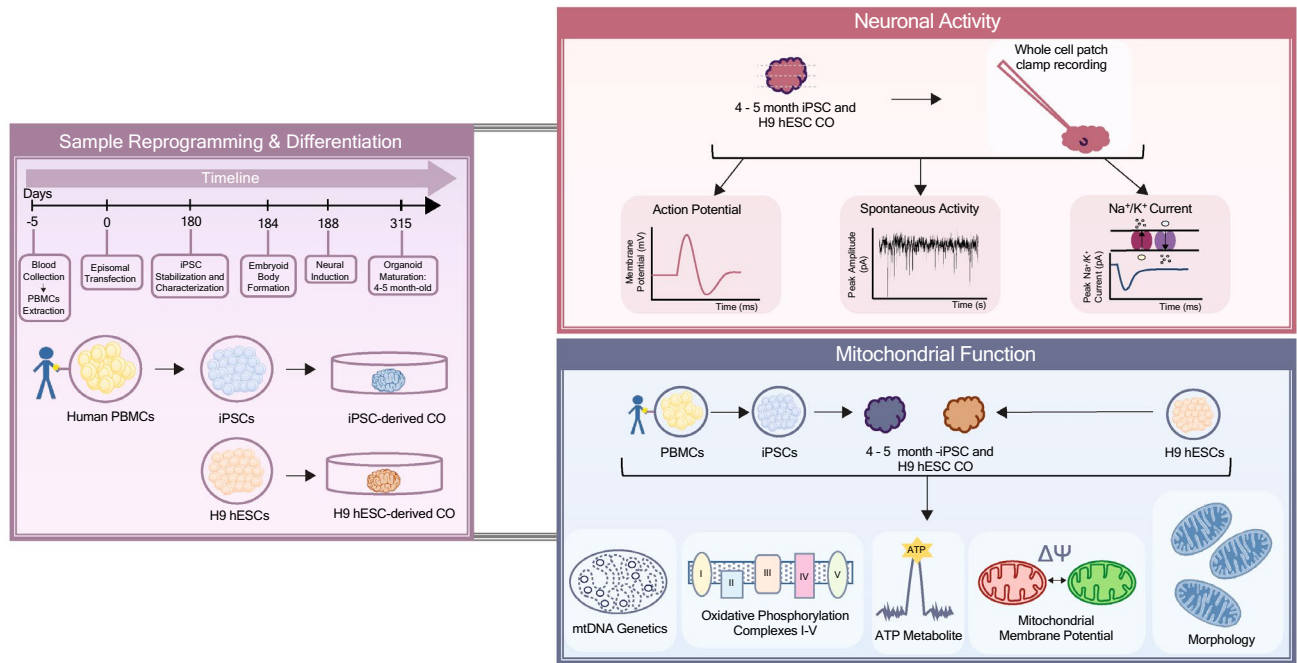
Figure 1. Schematic summary of the study design. Purple panel: An overview and a timeline of sample reprogramming and differentiation from peripheral blood mononuclear cells (PBMCs) to induced pluripotent stem cells (iPSCs) to cerebral organoids (COs) or H9 human embryonic stem cells (H9 hESCs) to COs. Red panel: An overview of electrophysiology experiments (action potentials, spontaneous activity, and sodium and potassium currents) in cerebral organoids. Blue panel: An overview of mitochondrial (mt-) genetics (mtDNA haplogroup, heteroplasmy and copy number), function (oxidative phosphorylation, ATP production and mitochondrial membrane potential) and morphology assessment across PBMCs to iPSCs to COs or H9 hESCs to COs.

them a unique and powerful tool for disease modelling and evaluation of mitochondrial health and neuronal activity[10,11]. COs have already been developed and extensively characterized using induced pluripotent stem cells (iPSCs) derived from human dermal fibroblasts[11–13]. However, this approach has drawbacks. Obtaining fibroblasts from the skin is an invasive and painful procedure. As well, dermal fibroblasts exhibit slow turnover and renewal rates and may potentially have accumulated environmentally-associated mitochondrial DNA mutations (such as those caused by ultraviolet radiation exposure from the sun) that may not reflect the underlying biology of the patient[14]. In contrast, obtaining peripheral blood mononuclear cells (PBMCs) from whole blood is a much easier and less invasive means of obtaining biological samples from patients. Due to their rapid turnover and self-renewal rates, constant circulation throughout the body, and lifetime immunological memory[15], COs generated from PBMCs may offer the advantage of more accurately representing the current disease state of the patient.

Here, we developed a human-derived CO model that allows for the assessment of mitochondrial health at the primary, reprogrammed, and differentiated stages, using iPSCs derived from PBMCs and compared and validated these by comparison to COs derived from human embryonic stem cells (hESCs; Fig. 1, Schema). Characterization of fully functional and preserved mitochondrial health throughout the differentiation to COs is crucial to moving toward understanding their role in brain development and disease. The use of PBMCs is flexible and straightforward compared to the use of fibroblasts obtained from invasive biopsies. We expect our approach to be a starting point for more sophisticated patient-derived brain models to investigate mitochondrial health and neuronal activity in a wide range of human diseases—a way forward in developing a standard of care for mitochondrial medicine.

Results

Generation of cerebral organoids using iPSCs derived from PBMCs. To determine whether a blood sample can be used to make COs (Fig. 2A), we first collected whole blood from a healthy female subject (Table S1 for clinical characteristics). PBMCs from whole blood were isolated using Ficoll density centrifugation and electroporated with episomal vectors expressing five reprogramming factors (Oct4, Sox2, Klf4, L-Myc and Lin28, Fig. 2A,B-i). An episomal method was chosen because it has been proven to be the most efficient method for generating integration-free human iPSCs from the blood[16]. We confirmed an apparently normal human, female karyotype in the resulting iPSCs (Fig. 2B-ii), indicating that genetic characteristics were retained during the reprogramming process and corresponded to the parental PBMC lineage. Immunofluorescence staining of iPSCs showed positive expression of key pluripotent proteins (Fig. 2B-iii and iv and Table S2). At the mRNA

level, pluripotent markers in the iPSCs were similar to those observed in H9 hESCs (Fig. 2B-v), further demonstrating successful generation of iPSCs from PBMCs.

We previously established a robust protocol that allows for the reproducible production of COs from human pluripotent stem cells[17]. These COs display consistent cell type composition and proportions across different batches, making this CO platform useful for disease research as it addresses the problem of variability[17]. Using this protocol, we generated 4.5-month old COs from PBMCs-derived iPSCs (N = 14, Table S3) and demonstrated that they have similar overall morphology as those derived from the H9 hESCs (N = 14, Fig. 2C and Fig. S1-A). Immunofluorescence staining of the histological sections showed the presence of radial glia (SOX2) and mature neuronal (NeuN) cell types in iPSC-derived COs, which were also present in H9 hESC-derived COs (Fig. 2D and Table S4 for replicates). These qualitative imaging results confirm successful in vitro differentiation of iPSCs derived from human PBMCs into COs. As a routine quality control to monitor the genomic integrity across the production stages (PBMCs, iPSC, iPSC-derived CO), we performed a simple sex characterization experiment and demonstrated no change to the female genomic DNA (Fig. S1-B, Tables S5 and S6), allowing us to use these COs for downstream investigation.

Mitochondrial genetics, function and morphology from PBMCs, iPSCs to COs.

Mitochondrial function has been classified as a key indicator of neuronal activity and healthy cells. Thus, we next monitored the integrity and stability of mitochondrial genotype, function and morphology across the primary (PBMCs), reprogrammed (iPSCs), and differentiated (COs) stages (Table S4 for replicates).

Mitochondria harbours its own genome in multiple copies, called the mitochondrial DNA (mtDNA). The mtDNA encodes required subunits of the electron transport and oxidative phosphorylation complexes as well as the ribosomal and transfer RNAs required for their translation[18]. As a result, it is critical to evaluate whether mtDNA integrity is preserved throughout the process of generating COs[19]. The integrity of mtDNA can be evaluated by identifying the: (1) haplogroup, which is defined by a set of genetic variants associated with maternal ancestry; (2) percentage of heteroplasmy (mix of normal and mutated mtDNA) or homoplasmy (uniform collection of mtDNA, either mutated or normal) and; (3) copy number.

Using mtDNA sequencing, we identified the X2g haplogroup across PBMCs, iPSCs and iPSC-derived COs (Fig. 2E, Tables S7, S8). We further validated these results by performing polymerase chain reaction (PCR) amplification of short mtDNA fragments corresponding to the X2g haplogroup and sequencing these products (Table S9). No change to the mtDNA haplogroup was observed (Table S8), confirming that the mitochondrial ancestry of the donor was retained throughout the process of CO production. The mtDNA is also susceptible to oxidative damage and lack protective histones, which could potentially lead to novel mutations in the iPSCs and COs[20]. To ensure the preservation of mtDNA integrity throughout the CO production, we evaluated the complete mtDNA sequence and confirmed that the nucleotide identity across PBMCs, iPSCs and iPSC-derived COs is 100%. As no novel mutations were introduced, these results assure that we have retained the mtDNA identity of the donor during the reprogramming and differentiation process. A recurring question in the scientific community is whether there is a selection process that drives homoplasmy from heteroplasmy upon iPSC reprogramming[21–23]. Using the mtDNA sequencing data, we demonstrated the conservation of four heteroplasmic variants across PBMCs, iPSCs and iPSC-derived COs suggesting no selection process occurred (Fig. 2E). To further evaluate mtDNA integrity, we performed quantitative polymerase chain reaction (qPCR) using specific primers that target a highly conserved gene in the mtDNA (NADH dehydrogenase subunit 1, MT-ND1) and quantified the ratio of MT-ND1 gene copy to two copies of a single-copy nuclear gene (Beta-2-Microglobulin, b2M). Our results revealed multiple copies of mtDNA, which were preserved upon CO production from iPSCs (Fig. 2E, Table S10). Altogether, we provided solid evidence that the iPSC-derived COs retained the mtDNA genetic identity of their somatic origin (PBMC), resulting in the recapitulation of the donor's mitochondrial phenotype.

While mtDNA integrity was preserved, a remaining question is whether this translates to healthy and functional mitochondria. As a first approach, we stained COs before and after differentiation using MitoTracker Red CMXRos, which is a cationic fluorescent dye that penetrates solely into active and live mitochondria in a potential-dependent manner. Following sample staining, we demonstrated MitoTracker-positive cells across PBMCs, iPSCs and iPSC-derived COs, which were similarly detected in H9 hESCs and H9 hESC-derived COs (Fig. 3A). As the mitochondria appeared live and active, we next investigated function and responsiveness. The functional state of the mitochondria can be evaluated by monitoring changes in the mitochondrial membrane potential (MMP)[24]. JC-1 (5,5′,6,6′-tetrachloro-1,1′,3,3′-tetraethylbenzimi-dazolylcarbocyanine iodide) is a dual emission cationic dye that accumulates in the mitochondria in response to the MMP, yielding a green fluorescence in less energetic mitochondria and red fluorescent aggregates in highly energetic mitochondria. Here, we used JC-1 dye as it is optimal for the end-point analysis of mitochondrial health[25]. Treatment of the H9 hESC- and iPSC-derived COs before and after differentiation with JC-1 led to an increased red-to-green fluorescence ratio, indicative of higher MMP, corresponding to a highly energetic mitochondrial state (Fig. 3B and Fig. S2-A). We next investigated whether these COs, both before and after differentiation, remained responsive to pharmacological intervention. For this, we administered carbonyl cyanide-4-(trifluoromethoxy)phenylhydrazone (FCCP), an uncoupler of oxidative phosphorylation (OXPHOS) that collapses and depolarizes the MMP to serve as our depolarization control. Treatment with FCCP led to a marked decrease in the red-to-green fluorescence ratio and fragmentation of the mitochondrial tubular network into smaller circular monomers (Fig. 3C and Fig. S2-A), indicating that in all cases, the COs are responsive to pharmacological intervention. Overall, these data demonstrate that the mitochondria remained functional and responsive throughout the process of generating COs.

The MMP is generated upon the passing of electrons through a group of mitochondrial protein complexes I, III, and IV located on the inner mitochondrial membrane, which in turn is used to drive adenosine
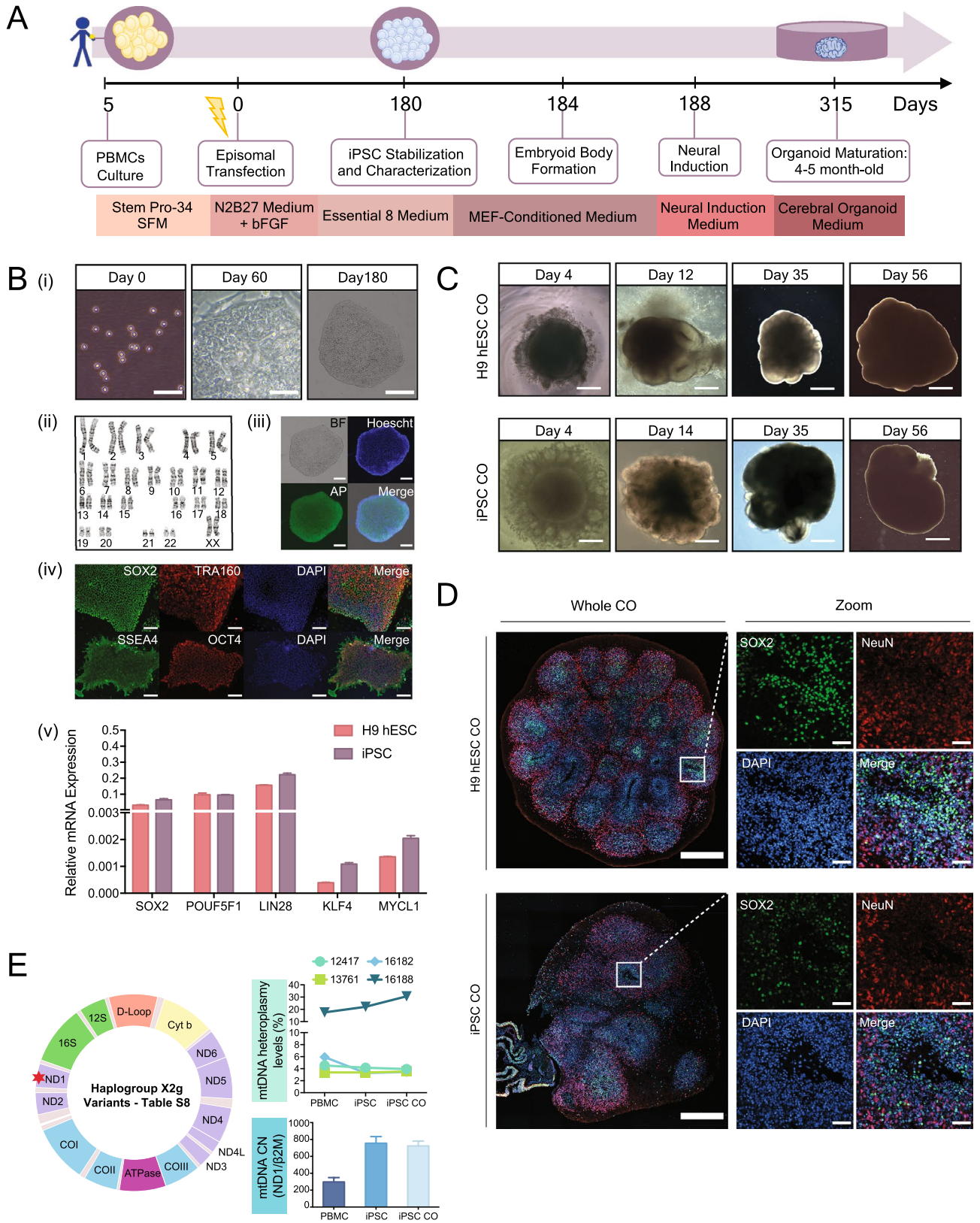
◄**Figure 2.** Generation and characterization of cerebral organoids from PBMCs-derived iPSCs and H9 hESCs. (**A**) Timeline and protocol schematic from peripheral blood mononuclear cells (PBMCs) to induced pluripotent stem cells (iPSCs) to cerebral organoids (COs). (**B**) (i) Representative bright-field images showing PBMCs on Day 0, scale bar, 50 μm, reprogramming iPSCs on Day 60, scale bar, 50 μm, and a fully stabilized iPSC colony on Day 180, scale bar, 200 μm; (ii) chromosome analysis with normal female karyotype (46, XX) in 20 cells examined; (iii) representative fluorescent images of iPSCs stained positive for alkaline phosphatase, scale bar, 100 μm; (iv) representative immunofluorescent images of iPSCs stained positive for a set of pluripotency markers, SOX2, TRA160, SSEA4 and OCT4, scale bar, 600 μm; (v) Bar graph showing relative mRNA expression of pluripotency markers, *SOX2*, *POUF51*, *LIN28*, *KLF4* and *MYCL1*. Bars, mean ± SD. (**C**) Representative bright field images showing the progression of cerebral organoid development in H9 hESCs (top panel, scale bars, 250 μm, 250 μm, 500 μm and 1 mm from left to right) and iPSCs (bottom panel, scale bars, 250 μm, 500 μm, 500 μm and 1 mm from left to right). (**D**) Representative fluorescent immunohistochemistry images of whole cerebral organoid in 4.5-month H9 hESC CO and iPSC CO section view (scale bar, 500 μm) and magnified view (scale bar, 50 μm) expressing nuclei (DAPI), radial glia (SOX2) and mature postmitotic neurons (NeuN). Note that immunofluorescent images were used for qualitative observations. (**E**) Mitochondrial (mt-) DNA haplogroup, heteroplasmy and copy number (CN) characterization across PBMCs, iPSCs and iPSC COs. Top right: graph showing mtDNA heteroplasmy levels at four nucleotide positions (MT-12417, MT-13761, MT16182 and MT-16188). Bottom right: graph showing relative mtDNA CN, expressed as MT-ND1/β2M ratio. Schematic of the mitochondrial DNA (left). Red star denotes the mtDNA region used to evaluate mtDNA CN. For more information on the haplogroup X2g variants, see Table S8.

5′-triphosphate (ATP) production through complex V. We determined the ability of COs derived from iPSCs and H9 hESCs to perform OXPHOS by measuring the assembly levels of intact mitochondrial complexes and the intracellular ATP levels. Using Luminex bead-based multiplex immunoassay, we successfully tracked the expression of intact mitochondrial complexes I–V across PBMC, iPSC and iPSC-derived COs and H9 hESC and H9 hESC-derived COs (Fig. 4A). To visualize the proper formation and distribution of OXPHOS, we performed immunofluorescence staining of TOMM-20, a marker of the outer mitochondrial membrane and NDUFS3, SDHA, UQCRC1, COX-IV, and ATP Synthase-β, markers of the inner mitochondrial membrane of complexes I, II, III, IV and V, respectively. We observed typical perinuclear mitochondrial distribution and expression (where clusters of mitochondria surround the nucleus) throughout the COs and cells (Fig. 4B and Table S2). To evaluate endpoint ATP levels that result from the balance between ATP production and usage, we performed CellTiter-Glo luminescent assay and shown the maintenance of ATP levels throughout the generation of COs, which was in a similar pattern to that observed for the OXPHOS data indicating high levels of endpoint ATP in stem cells as compared to COs (Fig. 4C and Fig. S2-B). Energy metabolism has been suggested to play a crucial role in the regulation and maintenance of pluripotency[26–28]. To examine this further, we used oligomycin, an inhibitor of complex V, to block ATP production by mitochondrial OXPHOS in PBMC-derived iPSCs and H9 hESCs. We observed a subtle decrease (~20%) in ATP levels (Fig. S2-C), suggesting that the immediate source of ATP is glycolysis in iPSCs and H9 hESCs. Although less efficient in terms of energy production, stem cells have been shown to use this pathway at a much faster rate which is crucial for maintaining pluripotency and may explain the high ATP levels[26,27,29]. In contrast, 4-month-old H9 hESC COs treated with oligomycin had a ~55% reduction in intracellular ATP, suggesting that COs utilize both OXPHOS and glycolytic pathways as their source of energy to at a similar extent (Fig. S2-C).

Lastly, we monitored mitochondrial number and visualized morphology using transmission electron microscopy (TEM). Consistent with OXPHOS and ATP production, H9 hESCs and iPSCs had higher number of mitochondria compared to their corresponding COs (Fig. 4D-i). Moreover, the electron micrographs revealed well-preserved mitochondrial morphologies with defined cristae before and after the generation of COs (Fig. 4D-ii). Consistent with expectations, mitochondria in the iPSCs and H9 hESCs displayed globular and immature shapes with electron-dense cristae whereas more elongated and mature mitochondria with thinner cristae were visually observed in the COs (Fig. 4D-ii), suggesting mitochondrial maturation during the differentiation process. While mature mitochondrial morphology was observed in COs, the source of ATP generation was not entirely dependent on OXPHOS (Fig. S2-C), suggesting that metabolic shift may follow as the COs becomes progressively more mature.

Electrophysiological responses in iPSC-derived cerebral organoids. A major functional test of any neuronal preparation is the ability to form functional mature neurons with active synaptic neurotransmission[30]. These properties can be tested using electrophysiological recordings from individual neurons and analysis of their action potential (AP)-generation and synaptic activity. Whole-cell recordings were performed in acute slices prepared from COs derived from iPSCs and H9 hESCs (Fig. 5 and Table S4 for replicates). All recorded neurons (N = 26 cells for H9 hESC-derived COs and N = 29 cells for iPSC-derived COs) were divided into three types based on a combination of electrophysiological properties, specifically immature neurons (Type 1), developing neurons (Type 2), and mature neurons (Type 3). Type 1 neurons were immature, could not generate APs, had higher membrane resistance and lower capacitance (Table S11), and relatively small sodium and potassium currents triggered by depolarization (Fig. 5B). Spontaneous activity was not recorded in type 1 immature neurons. Both type 2 developing neurons and type 3 mature neurons were able to generate APs; however, type 2 developing neurons had smaller amplitude and slower kinetics when compared to type 3 mature neurons (Fig. 5A). Correspondingly, sodium and potassium currents were smaller in type 2 developing neurons compared to type 3 mature neurons (Fig. 5B). In addition, only type 3 mature neurons generated stable trains of
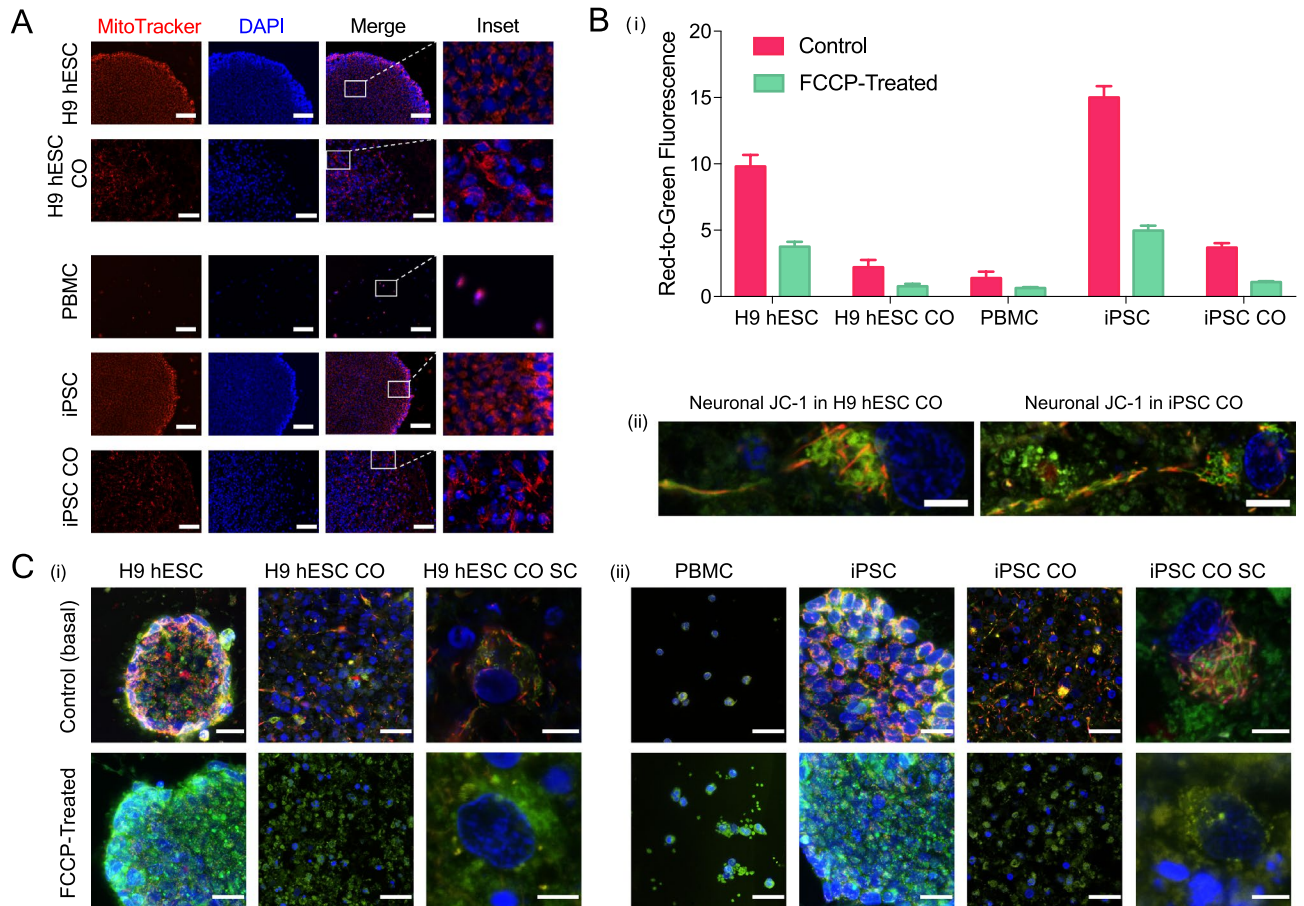
Figure 3. Characterization of active, functional and responsive mitochondria throughout CO generation. (**A**) Active mitochondria in H9 hESCs (scale bar, 100 μm), H9 hESC COs (scale bar, 50 μm), PBMCs (scale bar, 100 μm), iPSCs (scale bar, 100 μm) and iPSC COs (scale bar, 65 μm) stained with MitoTracker Red CMXRos (red) and DAPI (nuclei, blue). Last column shows insets, enlarged views of boxed areas from the merge images. (**B**) (i) Bar graph summarizing mitochondrial membrane potential (MMP) as red-to-green fluorescence ratio across primary, reprogrammed and differentiated stages in samples treated with JC-1 only (control basal MMP level) and those treated with carbonyl cyanide-4-(trifluoromethoxy)phenylhydrazone (FCCP). Fluorescence was recorded using a microplate reader. Bars, mean ± SD; (ii) Representative MMP images of a fully captured neuron with cell body and axon projection in H9 hESC CO (left, scale bar, 5 μm) and iPSC CO (right, scale bar, 7 μm). Red, JC-1 aggregates (highly energetic or polarized), green, JC-1 monomers (less energetic or depolarized). (**C**) (i) Top row shows representative MMP images across CO generation from H9 hESCs (scale bar, 25 μm) to H9 hESC CO (scale bar, 25 μm) or hESC CO single cell (SC, scale bar, 10 μm) and; (ii) from PBMCs (scale bar, 25 μm) to iPSCs (scale bar, 25 μm) to iPSC COs (scale bar, 25 μm) or iPSC CO SC (scale bar, 5 μm). Bottom row shows representative images of samples treated with FCCP followed by JC-1 to visualize the collapse of MMP in (i) H9 hESCs (scale bar, 25 μm) to H9 hESC CO (scale bar, 25 μm) or hESC CO SC (scale bar, 5 μm) and; (ii) from PBMCs (scale bar, 25 μm) to iPSCs (scale bar, 25 μm) to iPSC COs (scale bar, 25 μm) or iPSC CO SC (scale bar, 5 μm). All images were captured at ×100 magnification with slight variations in the zoom factor to capture the single cell(s) or single colony of interest. Immunofluorescent images shown here were used for qualitative observations only.

spontaneous APs at holding membrane level or during slight depolarization (Fig. 5C). However, spontaneous AP frequency and synaptic activity were similar between type 2 developing neurons and type 3 mature neurons (Fig. 5C).

Next, the electrophysiological properties of type 2 developing neurons and type 3 mature neurons in COs generated from PBMC-derived iPSCs were compared to those found in H9 hESC-derived COs. We found similar AP amplitude (Fig. 5A-ii) and rise time (Fig. 5A-iii) in type 2 developing neurons between the two types of COs. Type 2 developing neurons from iPSC-derived COs showed slower half-width (Fig. 5A-iv) and decay (Fig. 5A-v) while type 3 mature neurons showed no difference in any measured AP properties (Fig. 5A-i to v). In addition, the amplitude of sodium or potassium currents in type 2 developing neurons and type 3 mature neurons were similar between both types of COs (Fig. 5B). Finally, we showed similarities in spontaneous synaptic activity of type 2 developing neurons or type 3 mature neurons (Fig. 5C-ii and iii), and spontaneous AP frequency in type 3
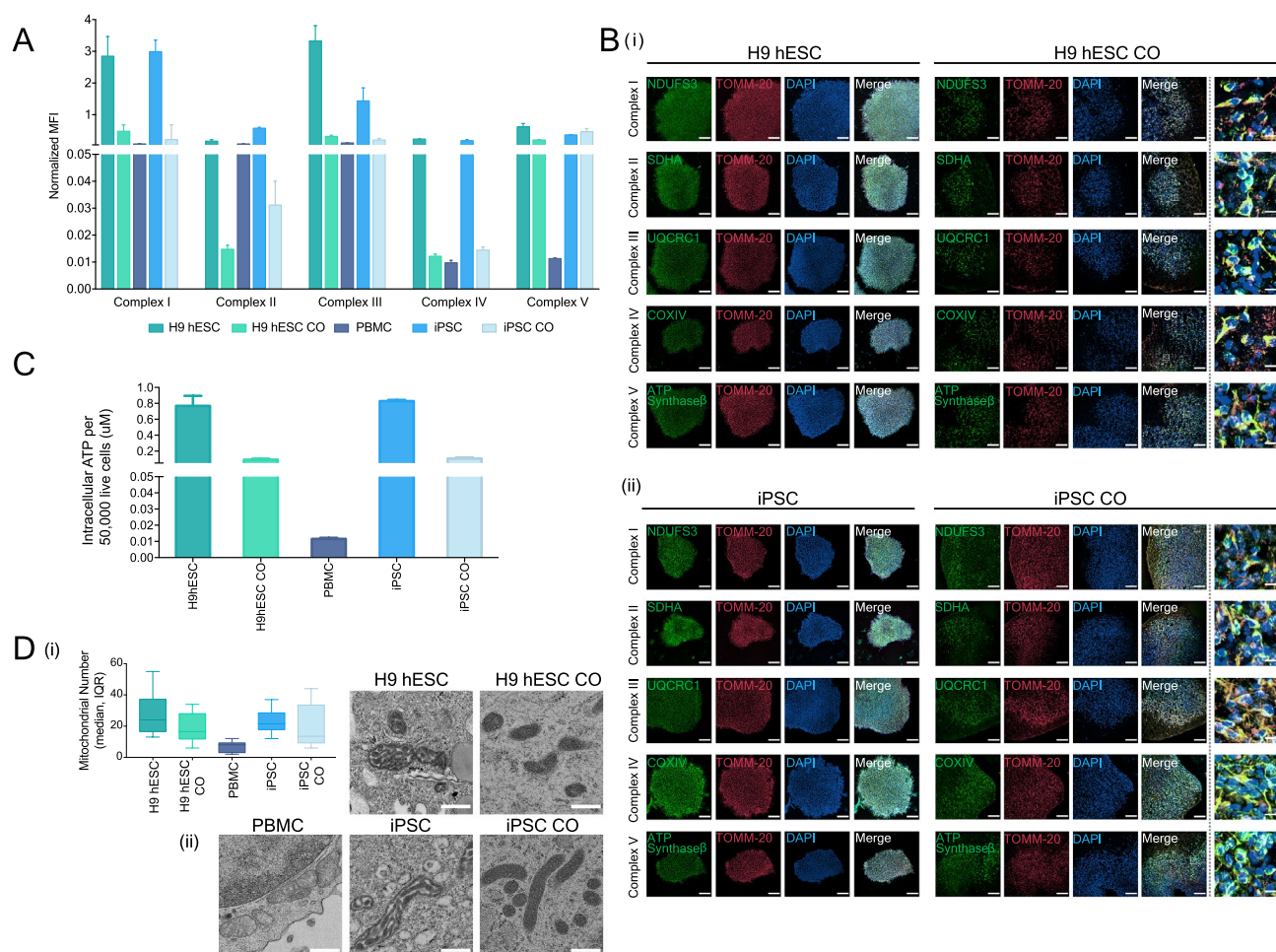
Figure 4. Mitochondrial oxidative phosphorylation and morphology throughout CO generation. (**A**) Bar graph showing the oxidative phosphorylation (OXPHOS) complexes I–V assembly levels in H9 hESCs, H9 hESC COs, PBMCs, iPSCs and iPSC COs. Median fluorescence intensities for each complex were recorded using Luminex technology. Bars, median fluorescence intensity ± SD. (**B**) Representative immunofluorescence images showing the formation of the inner mitochondrial membrane OXPHOS proteins (complex I, NDUFS3; complex II, SDHA; complex III, UQCRC1; complex IV, COXIV; complex V, ATP synthase-β; green) and the outer mitochondrial membrane (TOMM-20; red) in (i) H9 hESCs to H9 hESC COs and; (ii) iPSCs to iPSC COs. All scale bars, 100 μm. Last column shows insets, enlarged views of boxed areas from the merge CO images, all scale bars, 10 μm. In the CO tissues, out of focus light and autofluorescence of tissue matrix led to background noise which were corrected for better visualization. Brightness levels of each images were also adjusted to optimize visualization. Immunofluorescent images shown here were used for qualitative observations only—no quantitative analyses were performed. (**C**) Bar graph showing the intracellular ATP levels across H9 hESCs to H9 hESC COs and PBMCs, iPSCs to iPSC COs, bars, mean ± SD. (**D**) (i) Box plot summarizing the median number of mitochondria in 10 cells examined, boxes, median and interquartile range, IQR. (ii) Representative electron micrographs of mitochondrial morphology across H9 hESCs (scale bar, 5 μm) to H9 hESC COs (scale bar, 500 nm) and PBMCs (scale bar, 5 μm), iPSCs (scale bar, 500 nm) to iPSC COs (scale bar, 500 nm).

mature neurons (Fig. 5C-i), indicating that iPSC-derived COs contain mature neurons with electrophysiological properties similar to H9 hESC-derived COs.

Discussion

To the best of our knowledge, this is the first report demonstrating the development of a functional human-derived CO model made from PBMCs successfully tracking overall mitochondrial health, including genetics, function and morphology. Although the COs are immature, more closely resembling a fetal rather than an adult brain[31–34], they exhibited electrophysiological responses including both mature and immature neurons and displayed functional and responsive mitochondria across all stages of development, from PBMCs to iPSCs to iPSC-derived COs. We demonstrated the preservation of the donor's mtDNA genetic integrity, highlighting the potential of COs generated from PBMC-derived iPSCs to recapitulate the functional phenotypes that may be rooted in their genetic information. We further demonstrated the response of iPSC-derived COs to pharmacological
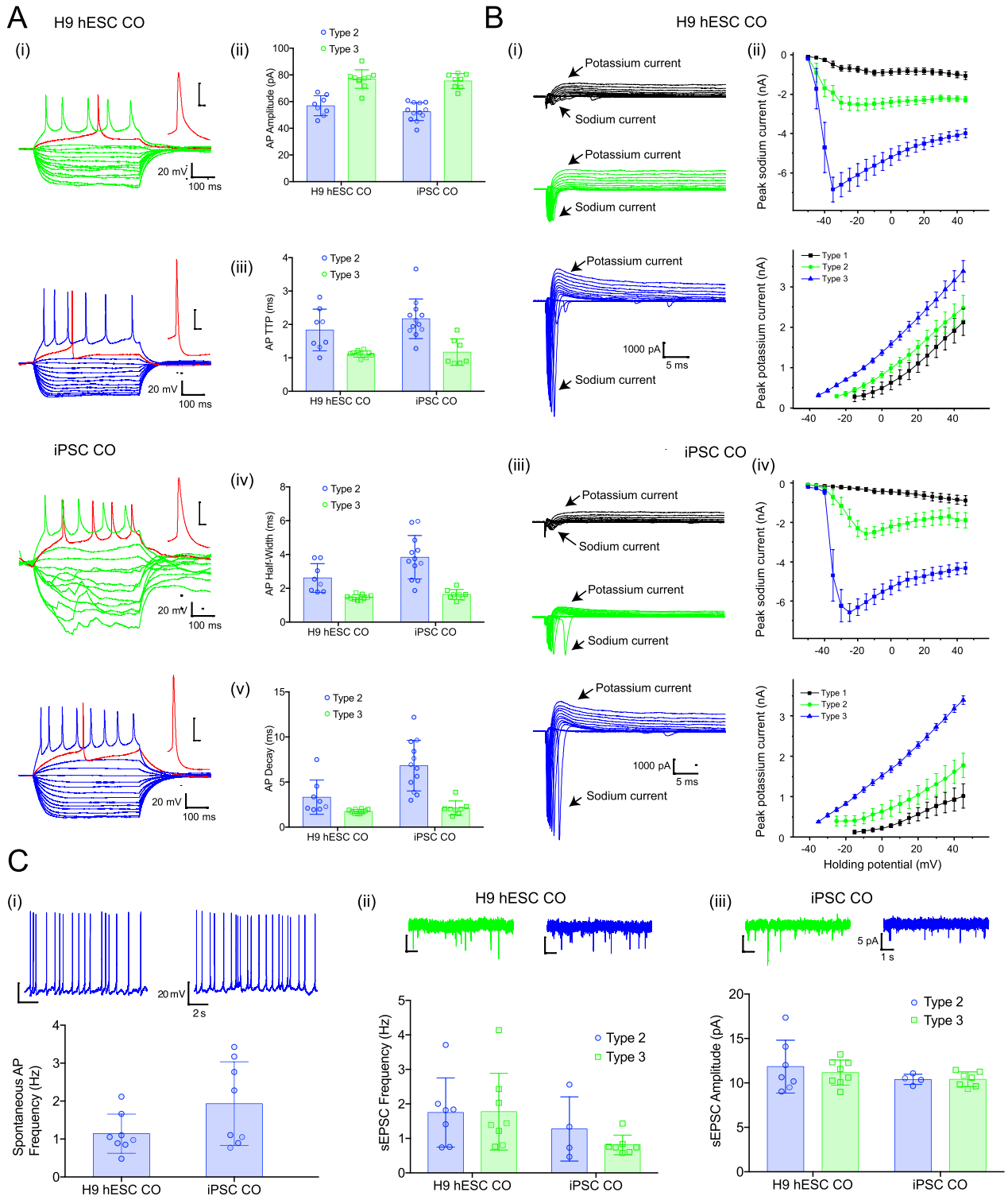
Figure 5. Electrophysiological characterization in H9 hESC-derived COs and iPSC-derived COs. (**A**) (i) Examples of voltage responses to hyperpolarizing and depolarizing set of currents recorded from type 2 (green) and type 3 (blue) neurons. Individual APs are expanded in the insert (red), scale 20 mV/5 ms. Summary bar graphs showing (ii) AP amplitudes, (iii) rise time, (iv) half-width and (v) decay, note that APs have lower amplitude and slower kinetic in type 2 neurons. (**B**) (i) Examples of inward sodium and outward potassium currents recorded from neurons type 1 (black), type 2 (green) and type 3 (blue). Scale bar is the same for all traces. Summary current–voltage plots showing increase in peak current amplitude for both sodium (top) and potassium (bottom) during neuronal maturation (ii and iii). These plots look similar independently of COs origin. (**C**) (i) Examples of spontaneous AP firing in type 3 neurons (top) and summary bar graph of AP frequency in H9 hESC- and iPSC-derived COs (bottom). (ii) Examples of spontaneous excitatory postsynaptic currents (EPSCs) recorded from type 2 (green) and type 3 (blue) neurons. Scale bar is the same for all traces. (iii) Summary bar graphs showing that spontaneous synaptic activity including sEPSC frequency (left) and amplitude (right) was similar in both types of neurons regardless origin of COs. Error bars show standard deviation.

treatment (FCCP), mimicking the individual's overall cellular/mitochondrial response, which supports the use of iPSC-derived COs as a representative model to evaluate function and to screen for therapeutic compounds.

Despite encouraging progress, CO models do have limitations. An ongoing challenge is that with prolonged culture, COs reach a size limit along with the occurrence of cell death in the centre regions due to insufficient diffusion of oxygen and nutrients[11,35]. While it may be possible to increase oxygen availability by growing COs in a higher oxygen environment, this can be toxic if not carefully controlled[36]. So far, COs do not develop vasculature that could provide nutrients, but studies involving vascularization, generation of blood vessel organoids, and the development of microfluidics are underway and have yielded some promising results[37–39]. With these technological advancements, we expect that mitochondrial maturation will follow during the CO maturation process and become progressively more OXPHOS dependent on energy production. Without these technological advancements, COs remain immature and do not mature past the prenatal stage. As such, the COs currently on the research market are only beneficial in investigating mitochondrial dysfunction during early neurodevelopment in the brain of diseases that may have an underlying neurodevelopmental origin.

Furthermore, the long-term culture required for the maturation of COs to 4.5 months limits the amount of material available for screening. This issue can delay the clinical process of diagnostic and therapeutic development and turnaround time. Thus, future studies are needed to develop methods that will allow these organoids to fully and rapidly mature into an adult brain to allow for high throughput mitochondrial diagnostics and therapeutic development in a clinical context. Next, we only evaluated mitochondrial health at the whole tissue level at one time point as an initial proof-of-concept; however, energy production and consumption can vary amongst different cell types in the brain. As a result, future studies are needed to sort the cells and evaluate mitochondrial function in different cell types within the COs and at other time points. Finally, we are aware that respirometry approach is the gold standard and widely used to evaluate mitochondrial function in cells. However, respirometry techniques are currently standardized in two-dimensional single-cell systems and not three-dimensional COs above 500 μm in size due to the size limitations of the measurement chamber (Agilent Technologies, Inc). While using single cells from dissociated COs has been proposed, the loss of three-dimensional interconnection between neurons and different cell types, as well as subsequent single cell culturing can affect the viability and cellular behaviour, which in turn can affect the interpretation of the data. With these limitations in mind, future work is warranted to overcome these technological limitations.

While acknowledging that CO models currently do not have the full precision of a human brain, the ability to interrogate overall mitochondrial health in a human context is extremely valuable for studying brain development and diseases. By evaluating mitochondrial health in both the PBMCs and iPSC-derived COs, we can start to identify changes in the brain that may also be present in the blood of patients. As a result, this approach can aid in the development of biomarkers, companion diagnostics, and novel mitochondrial therapeutics that can inform critical clinical decisions in mitochondrial medicine. As there is currently no standard of care for the assessment of mitochondrial health in both the brain and peripheral blood of patients, the platform provided here is a potential starting point that can be applied to a wide range of human diseases.

Materials and methods

Blood sample collection and processing.   We followed the guidelines established by the Biomarkers Task Force as modified by the World Federation of Societies of Biological Psychiatry for clinical assessment and documentation, ethical procedures and blood sample collection[40]. This study was performed in accordance with the latest version of the Declaration of Helsinki and approved by the Research Ethics Board at the University of Toronto, Canada (Protocol Number: 29949). Informed consent of the participant was obtained after the nature of the procedures had been fully explained. Venous blood (10 mL) was drawn from a participant through venipuncture into a plastic whole-blood tube with spray-coated K_2EDTA (16×100 mm $\times 10.0$ mL BD Vacutainer Plus). Whole blood was carefully layered on Ficoll-Paque (GE Healthcare, 17144002) at a 1:1 ratio in a conical tube and centrifuged at $400 \times g$ for 40 min. Following centrifugation, peripheral blood mononuclear cells (PBMCs) from the buffy coat were isolated, washed twice with Dulbecco's phosphate-buffered saline (DPBS) (Gibco, 14190250), and immediately seeded in a 25 cm² tissue culture flask at a density of about 2×10^6 cells containing 10 mL of StemPro-34 SFM (Gibco, 10639011) supplemented with GlutaMAX-I (1X), recombinant human SCF (100 ng/mL), recombinant human IL-3 (50 ng/mL), and recombinant human GM-CSF (25 ng/mL) for 72 h at 37 °C with 5% CO_2.

Generation of induced pluripotent stem cells.   PBMCs were transfected with Epi5 EBNA-1/OriP-based episomal vectors containing five pluripotent factors (Oct4, Sox2, Klf4, L-myc and Lin28) using the Neon Transfection System (Invitrogen, A15960) following the manufacturer's protocol. Briefly, PBMCs at a density of 2×10^5 per mL were suspended in the buffer supplied by the manufacturer. Equal amounts (1 μg) of Epi5 reprogramming and the Epi5 p53-EBNA vectors were used to transfect the PBMCs via electroporation by setting the parameters to 1650 V, 10 ms and 3 pulses. Following transfection, PBMCs were distributed into preconditioned plates coated with 1:50 Geltrex LDEV-Free, hESC-Qualified, Reduced Growth Factor Basement Membrane Matrix (Gibco, A1413302) containing StemPro-34 SFM (Gibco, 10639011) media supplemented with GlutaMAX-I (1X), recombinant human SCF (100 ng/mL), recombinant human IL-3 (50 ng/mL), and recombinant human GM-CSF (25 ng/mL). After 24 h of incubation at 37 °C with 5% CO_2, cells were transitioned to N2B27 media, composed of DMEM/F-12, HEPES, N-2 Supplement (1X), B-27 Supplement (1X), MEM Non-Essential Amino Acids Solution (1X), GlutaMAX-I (0.5X), 2-Mercaptoethanol (1:500), FGF-Basic (AA 1–155) Recombinant Human Protein (100 ng/mL). N2B27 media was changed every other day with fresh FGF-Basic (100 ng/mL) until emergence of reprogramming induced pluripotent stem cells (iPSC) colonies. iPSC colonies

that exhibited embryonic stem cell (ESC)-like morphologies were picked under a stereomicroscope for expansion and maintenance in Essential 8 medium (Gibco, A1517001).

Characterization of induced pluripotent stem cells. We followed the workflow developed by Marti et al. showing the different steps required to characterize an iPSC line, which includes: (1) pluripotency test (alkaline phosphatase and immunodetection of pluripotency markers) and (2) karyotype[41].

Alkaline phosphatase live stain. iPSCs were stained with Alkaline Phosphatase (AP) Live Stain (Invitrogen, A14353) as per the manufacturer's protocol. iPSCs cultures were incubated with AP Live Stain diluted at 1:500 in DMEM/F-12, HEPES media for 30 min at 37 °C with 5% CO_2 and 2 drops/mL of NucBlue Live ReadyProbes Reagent (Invitrogen, R37605) for 20 min. Following staining, cells were washed twice with DMEM/F-12, HEPES media (5 min per wash) to remove excess substrate. After the final wash, FluoroBrite DMEM (Gibco, A1896701) media was added and iPSCs were immediately visualized using the EVOS FL Cell Imaging System (Invitrogen).

Detection of pluripotency markers. Protein expression of pluripotent markers (SSEA4, OCT4, SOX2, TRA-1-60) in iPSCs was performed using the Pluripotent Stem Cell 4-Marker Immunocytochemistry Kit (Invitrogen, A24881). iPSC colonies were fixed for 15 min, permeabilized for 15 min and blocked for 30 min at room temperature. Two primary antibody combinations were used to incubate the iPSCs: antibody combination 1: anti-SSEA4 and anti-OCT4; and antibody combination 2: anti-SOX2 and anti-TRA-1-60 for 3 h at room temperature. After washing, iPSCs were incubated with secondary antibodies (Alexa Fluor 594 donkey anti-rabbit for anti-OCT4, Alexa Fluor 488 goat anti-mouse IgG3 for anti-SSEA4, Alexa Fluor 488 donkey anti-rat for anti-SOX2 and Alexa Fluor 594 goat anti-mouse IgM for anti-TRA-1-60) for 1 h. Following wash, 1 drop of NucBlue fixed cell stain (DAPI; Invitrogen) was added, and images of iPSCs were captured using a Nikon Eclipse Epifluorescent microscope equipped with a 12-bit Q-imaging camera, Retiga 1300B (7323). To validate pluripotency at the messenger RNA (mRNA) level, we performed quantitative reverse transcription polymerase chain reaction (qRT-PCR). The experiment was performed using wet bench verified pre-designed RT² qPCR primers on SOX2, POUF5F1, KLF4, MYCL1, LIN28A and two reference genes (GAPDH and ACTB). Total RNA was extracted from the iPSCs and H9-hESCs using the RNeasy Mini Kit (Qiagen) as per the manufacturer's protocol. The cDNA was synthesized from 500 ng of total RNA following the Qiagen's RT² First Strand Kit. Each PCR reaction contained 1 μL cDNA mixture, 1 μL RT² qPCR primers (SOX2 or POUF5F1 or KLF4 or MYCL1 or LIN28A or GAPDH or ACTB), 10.5 μL of water, and 12.5 μL of RT² SYBR Green master mix. After 46 cycles of amplification, data was acquired using BioRad CFX96 RT-PCR detection system with the following cycling conditions: 1 cycle of 10 min at 95 °C to activate HotStart DNA Taq Polymerase and 45 cycles of 15 s at 95 °C, followed by 1 min at 60 °C for fluorescence data collection. The expression level of each gene of interest was normalized to the housekeeping gene and was expressed as mean $2^{-\Delta CT}$ or $2^{-[CT \text{ (gene of interest)} - CT \text{ [GEOMEAN(GAPDH, ACTB)]}]}$.

Karyotype. Karyotype analysis via G-banding was performed on cells from two 25 cm² tissue culture flasks submitted to the TCAG Cytogenomics Facility. When cells reached 50% confluence, Karyomax Colcemid was added to each flask to a final concentration of 0.15 μg/mL (Cat. #15212-012, Gibco, CA, USA) and incubated in 37 °C CO_2 incubator for 1 h for one flask, and 30 min for the second flask. Cells were then collected by treating with 1 mL 0.05% trypsin, 0.53 mM EDTA (Cat. #325042 EL, WISENT Inc., Quebec, Canada) at 37 °C for 5 min, and pipetted up and down five times to break into single cells. Cells from each flask were centrifuged in a 15 mL conical tube at 200×g for 10 min, supernatant was aspirated until 0.5 mL remained, and cell pellet was flicked to resuspend completely. Cells were suspended in 8 mL buffered hypotonic solution (0.054 M KCl, 0.02% EGTA, 20 mM HEPES, pH 7.4), and incubated in 37 °C for 25 min. Eight drops of Carnoy's fixative (methanol/acetic acid, 3:1) were added and mixed together. Cells were centrifuged at 200×g for 10 min, supernatant was aspirated until 0.5 mL remained, and cell pellet was flicked to resuspend completely. Carnoy's fixative was added to the 14 mL mark, tubes were inverted to mix, and incubated in − 20 °C for at least one hour to overnight. After two more rounds of fixations (add 8 mL fixative, invert to mix, and centrifuge at 200×g for 10 min), cells were resuspended in 0.5–1 mL of fixative and cells from each suspension were dispensed onto glass slides and baked at 90 °C for 1.5 h, followed by overnight aging at room temperature in desiccator. Routine G-banding analysis was then carried out. Twenty metaphases per cell line were examined.

Generation of cerebral organoids from H9 hESCs and iPSCs. Cerebral organoids were generated from iPSC and H9 hESCs as previously described[17]. In brief, stem cells were aggregated into embryoid bodies and after induction of the neural germ layer were embedded in Matrigel droplets in differentiation media. Once removed from the Matrigel, free-floating organoids were maintained in prolonged culture on an orbital shaker.

Fluorescent immunohistochemistry for the characterization of cerebral organoids. Whole COs derived from H9 hESCs and iPSCs were fixed with 4% paraformaldehyde at 4 °C overnight on an orbital shaker, cryoprotected in 30% (weight/volume) sucrose at 4 °C overnight and embedded in optimal cutting temperature compound. Cryosections of 14 μm thickness were collected on Superfrost Plus Microscope glass slides (Fisher Cat# 12-550-15) using a Leica cryostat and were stored in − 80 °C until analysis. Prior to immunofluorescent staining, cryoslides from H9 hESCs- and iPSCs-derived COs were equilibrated to room temperature and tissues were rehydrated with 0.1% Tween-20 in 1X PBS pH 7.4. Tissues were then incubated in permeabilization/blocking solution (1X PBS pH 7.4, 10% Normal Donkey Serum, 2% BSA, 0.5% Triton X-100) for 1 h at RT in a humidified chamber. Proteins of interest were labeled with the following primary antibodies: SOX2 (goat, R&D,

AF2018, 3 µg/mL) and NeuN (rabbit, Cell Signaling Technology, 12943S, 1:500) diluted in antibody blocking solution (1X PBS pH 7.4, 0.1% Tween-20, 1% BSA, and 5% Normal Donkey Serum) at 4 °C and incubated overnight in a humidified chamber. Following overnight incubation, tissues were washed three times (5 min per wash) with 0.1% Tween-20 in 1X PBS pH 7.4 and then incubated overnight at 4 °C with the appropriate secondary antibodies: Donkey anti-Goat IgG (H + L) Highly Cross-Adsorbed Secondary Antibody Alexa Fluor Plus 555 (Invitrogen, A32816) and Donkey anti-Rabbit IgG (H + L) Highly Cross-Adsorbed Secondary Antibody Alexa Fluor Plus 647 (Invitrogen, A32795) diluted 1:750 in antibody blocking solution. Following secondary antibody incubation, tissues were washed three times in 1X PBS pH 7.4 with 0.1% Tween-20. Nuclei were counterstained by adding a small drop of ProLong Gold Antifade Mountant with DAPI (Invitrogen, P36935) to each tissue section prior to sealing under glass coverslips. Mountant was left to cure overnight at room temperature and protected from light. Images were captured using Leica TCS SP8 lightning confocal laser scanning microscope (DMI6000) equipped with white light laser (470–670 nm). Z-stack images were taken at 1 µm intervals and images were collected using LASX software (Lecia Microsystems). See Table S4 for biological and technical replicates.

Acute slice preparation.   Brain organoids (4.5 months old) were embedded into 4% low melting agarose and 300 µm slices were cut with vibrating-blade microtome (Leica, Germany). Slices were prepared using ice-cold artificial cerebrospinal fluid (ACSF) containing (mM): NaCl 87, NaHCO$_3$ 25, KCl 2.5, NaH$_2$PO4 1.25, MgCl$_2$ 7, CaCl$_2$ 0.5, glucose 25 and sucrose 75. Right after sectioning, slices were placed in oxygenated ACSF at room temperature and used for experiments within 4 h. All recordings were performed with extracellular ACSF containing (mM): NaCl 124, NaHCO$_3$ 25, KCl 2.5, MgCl$_2$ 1.5, CaCl$_2$ 2.5 and glucose 10, equilibrated with 95% O$_2$–5% CO$_2$, pH 7.4, maintained at 29–32 °C and perfused at a rate of 2–3 mL/min.

Electrophysiology.   Whole-cell current-clamp and voltage-clamp recordings were made with glass electrodes (3–5 MΩ) filled with a solution containing (mM): K-gluconate 120, KCl 20, MgCl2 2, EGTA 0.6, MgATP 2, NaGTP 0.3, Hepes 10, phosphocreatine 7. Individual neurons were visually identified usually around slice edge in order to increase chance of patching mature neurons. Electrophysiological recordings were made using a Multi Clamp 700A amplifier (Axon Instruments, Union City, CA, USA), operating under current-clamp and voltage-clamp mode. Data were filtered at 4 kHz, and acquired using pClamp 10 software (Molecular devices, Sunnyvale, CA, USA). All recordings were done at a holding potential − 70 mV. The uncompensated series resistance was monitored by the delivery of − 10 mV steps throughout the experiment, only recordings with less than 15% change were analyzed.

Resting membrane potential was measured immediately after establishing whole-cell patch clamp recording and followed by measurements of passive neuronal properties (access resistance, membrane resistance and capacitance) using automatic membrane test in pClamp 10 software. Ability to generate spontaneous action potentials was tested in current clamp mode starting from holding membrane potential and by application of depolarizing steps (5 pA increments) until steady firing was reached. This steady firing was observed only in mature neurons. Voltage-dependent sodium and potassium currents were measured in voltage clamp mode, using 500 ms voltage steps applied from a holding potential to a range of potentials between − 50 and + 50 mV (in 10 mV increments). Action potentials were triggered using 500 ms depolarizing pulses increasing amplitude (in 5 pA steps). Synaptic events were analyzed using pClamp 10 software within 5 min of recordings, individual events were detected using automatic template search. Templates were created using the average of at least 10 events aligned by the rising of their slopes. AP amplitude, rise time, half width and time to peak (TTP) were calculated to investigate excitability. See Table S4 for biological and technical replicates.

Total DNA extraction.   Genomic DNA was isolated from PBMCs, stem cells (H9 hESCs and iPSCs) and COs derived from H9 hESCs and iPSCs using the QIAamp DNA Mini Kit (Qiagen, 51304) by following the manufacturer's recommended protocol and using the recommended elution volumes. The concentration, purity and integrity of all extracted DNA was determined by spectrophotometric measurement on the NanoDrop ND-1000 (Thermo Fisher Scientific).

Sex and haplogroup characterization.   Primer pairs for haplogroup and sex determination (which included a genomic control primer pair) are listed in Tables S5, S6 and S9. PCR reactions for sex determination or haplogroup were performed on 5–10 ng genomic DNA in a 25 µl reaction mix containing 16.6 mM (NH4)$_2$SO$_4$, 67 mM Tris–HCl pH 8.8, 6.7 mM MgCl$_2$, 5 mM 2-Mercaptoethanol, 6.7 mM EDTA, 10% Dimethyl-sulfoxide, 0.125 mg/ml Bovine Serum Albumin (Bioshop), 1 mM each deoxynucleotide triphosphate (Biobasic), 0.5 µM each primer (IDT) and 1.5u DreamTaq (ThermoFisher). All of the amplifications were performed on a BioRad C1000 thermal cycler. For the sex determination, the conditions were 96 °C for 2 min; 12 cycles of 94 °C for 20 s, 64–58 °C for 30 s (reducing 0.5 °C per cycle) and 72 °C for 35 s, followed by 28 cycles of 94 °C for 20 s, 58 °C for 30 s and 72 °C for 35 s with a final extension step at 72 °C for 5 min. For the haplogroup primers, the conditions were 96 °C for 1 min; 40 cycles of 94 °C for 30 s, 56 °C for 20 s and 72 °C for 150 s with a final extension step at 72 °C for 5 min. The PCR products for the sex determination were separated on a 1.8% TBE agarose gel containing 0.5 µg/ml Ethidium Bromide at 100 V and visualized under UV light. Ten PCR products for haplogroup sequencing were purified using Biobasic EZ-10 Spin Column PCR Products Purification Kit following the manufacturer's instructions and eluted in ddH$_2$O for sequencing with internal primers. Sequencing reactions were performed by The Centre for Applied Genomics (The Hospital for Sick Children) on ABI 3730XL machines.

Mitochondrial DNA sequencing for haplogroup and heteroplasmy characterization. The mitochondrial DNA was amplified as two fragments using two the following two primer sets: (1) COIII-F (5′-TCA CAATTCTAATTCTACTGA-3′) and mt16425R (5′-GATATTGATTTCACGGAGGATGGTG-3′) resulting in a 7321 bp fragment and (2) mt16426F (5′-CCGCACAAGAGTGCTACTCTCCTC-3′) and COIII-R (5′-CGGATG AAGCAGATAGTGAGG-3′) and 10,011 bp products. PCR reactions were performed using TaKaRa LA Taq Hot Start polymerase kit (TaKaRa) and 50 ng of total genomic DNA in a 50 μL PCR reaction. Cycling conditions included an initial denaturation at 94 °C for 2 min, followed by 30 cycles of denaturation at 94 °C for 20 s, annealing at 60 °C for 30 s, and extension at 68 °C for 12 min. The reaction was concluded with a final extension at 68 °C for 20 min. PCR products were analyzed on an agarose gel and HindIII Ladder (New England Biolabs), and subsequently purified with the GeneJet PCR Purification kit (ThermoFisher). Samples were then submitted for Illumina sequencing Nextera XT library prep on a Hiseq 2500 high throughput flowcell 2 × 125 bp.

Mitochondrial DNA copy number. We adapted a protocol from Picard et al. for measuring relative mtDNA copy number by qPCR[42]. Relative mtDNA copy number was measured by calculating the ratio of MT-ND1 gene copy to two copies of a single-copy nuclear gene (β-2 microglobulin). As mtDNA quantification is relative (not absolute), the results presented here do not represent actual copy numbers. Briefly, total genomic DNA was extracted as described in the method "Total DNA Extraction" and diluted to 0.1 ng/μL. The ratio of mtDNA to nuclear DNA was quantified by $2^{-\Delta Ct}$ method using the following primer pairs: β-2 microglobulin forward (TGCTGTCTCCATGTTTGATGTATCT) (3′–5′) and reverse (TCTCTGCTCCCCACCTCTAAGT) for nuclear DNA, and ND1 forward (ATGGCCAACCTCCTACTCCT) and reverse (CTACAACGTTGGGGCCTTT T) for mtDNA. Each PCR reaction (20 μL) contained 2X SensiFAST SYBR No-ROX mix (Bioline, BIO-98005, 10 μL), 10 μM primers, and 0.6 ng of template DNA. After 40 cycles of amplification, data was acquired using BioRad CFX96 RT-PCR detection system (Bio-Rad Laboratories, Inc.) with the following cycling conditions: (1) 95 °C for 3 min; (2) 95 °C for 10 s and (3) 60 °C for 20 s. See Table S4 for biological and technical replicates.

MitoTracker live staining. Cerebral organoids (4.5 months old) were cut into 300 μm slices according to the methods described in "Acute slice preparation". CO slices were perfused at a rate of 2–3 mL/min in oxygenated MitoTracker staining solution containing: ACSF and MitoTracker Red CMXRos (Invitrogen, M7512, 100 nM) for 30 min at 29–32 °C in the dark. After washing three times, samples were fixed in 4% paraformaldehyde overnight at 4 °C. Sections of 300 μm thickness were embedded into 4% low melting agarose and further cut into 50 μm slices with vibrating-blade microtome (Leica, Germany). Nuclei were counterstained by adding a small drop of ProLong Gold Antifade Mountant with DAPI (Invitrogen, P36935) to each tissue section prior to sealing under glass coverslips. Mountant was left to cure overnight at room temperature and protected from light. Images were captured using Leica TCS SP8 lightning confocal laser scanning microscope (DMI6000) equipped with white light laser (470–670 nm). For imaging of MitoTracker Red CMXRos, 561 nm excitation was used, and emission was acquired at 595 nm by a hybrid detector. Z-stack images were taken at 1 μm intervals and images were collected using LASX software (Lecia Microsystems). For PBMCs and stem cells (iPSCs and H9 hESCs), cells were cultured on Geltrex-coated 6-well tissue culture plate (Starstedt, 83.3922.005). Cells were incubated in MitoTracker staining solution containing culture media and MitoTracker Red CMXRos (Invitrogen, 100 nM) for 30 min at 37 °C with 5% CO_2 in the dark. Following incubation, the staining solution was removed, and samples were washed three times (5 min per wash) with 1X PBS pH 7.4. After the final wash, FluoroBrite DMEM (Gibco, A1896701) media was added and PBMCs, H9 hESCs and iPSCs were immediately visualized using the EVOS FL Cell Imaging System (Invitrogen).

Single-cell dissociation of cerebral organoids. Whole COs were incubated in dissociation solution containing TrypLE Express (Invitrogen, 12604013) and 0.1 mg/mL of DNase I Solution (STEMCELL Technologies, 07900) for 1 h at 37 °C with 5% CO_2. During the 1-h incubation, COs were mechanically triturated (pipetted up and down 5 times) every 15 min to dissociate into single cells. At the end of digestion, the digest containing TrypLE Express was neutralized with 5 mL of CO media and the resulting cell solution was filtered twice by passing through cell strainers (Fisherbrand, 22363547, mesh size: 40 μM) attached to a conical tube to further create a single cell suspension. Cells were centrifuged for 200×*g* for 5 min, the supernatant was removed, and the cell pellet was resuspended in 1 mL of CO media for cell count using the Orflo Moxi Flow. The resulting number of cells were used for downstream mitochondrial functional analyses, including ATP and mitochondrial membrane potential measurements. Methods for these experiments are outlined below.

Mitochondrial membrane potential (MMP) assessment. *Live imaging for qualitative assessment.* Cerebral organoids (4.5 months old) were cut into 100 μm slices according to the methods described in "Acute slice preparation". Live tissue slices were mounted onto the coverglass bottom surface of 35 mm cell imaging dishes (Eppendorf, 145 μm thickness, 0030740009) coated with Cell-Tak Cell and Tissue Adhesive (Corning, CB40240, 3.5 μg/cm²). For PBMCs and stem cells (iPSCs and H9 hESCs), cells were cultured on Geltrex-coated cover glass of 35 mm cell imaging dishes (Eppendorf, 145 μm thickness, 0030740009). Samples were evaluated based on two conditions: basal MMP and inhibited MMP. To visualize basal MMP, samples were incubated in JC-1 staining solution containing culture media and JC-1 Dye (Invitrogen, Mitochondrial Membrane Potential Probe, T3168, 1 μg/mL) for 30 min and 2 drops per mL of NucBlue Live ReadyProbes Reagent (Invitrogen) for 20 min at 37 °C, 5% CO_2 in the dark. To visualize MMP inhibition, samples were treated with carbonyl cyanide 4-(trifluoromethoxy) phenylhydrazone (FCCP, abcam, ab120081) prepared in culture media at 100 μM concentration for 15 min at 37 °C, 5% CO_2 in the dark. Many research groups have used this high concentration to eliminate the MMP and JC-1 staining to serve as a depolarization control for JC-1, as well as provide an indica-

tion of cellular response to FCCP[43–47]. After FCCP treatment, samples were incubated in JC-1 staining solution for 30 min and 2 drops per mL of NucBlue Live ReadyProbes Reagent (Invitrogen, R37605) for 20 min at 37 °C, 5% CO_2 in the dark. Following staining, samples were washed three times (5 min per wash) with 1X PBS pH 7.4 to remove excess substrate. After the final wash, FluoroBrite DMEM (Gibco) media was added to the imaging dish and samples were immediately visualized using the Leica TCS SP8 lightning confocal laser scanning microscope (DMI6000) equipped with white light laser (470–670 nm) and stage-top humidified incubation system set at 37 °C and 5% CO_2. For imaging of JC-1 dye, 485 ± 11 nm excitation was used, and emission was acquired at 530 ± 15 and ≥ 590 nm by two hybrid detectors using LASX software (Lecia Microsystems). See Table S4 for biological and technical replicates.

Fluorescence spectroscopy for semi-quantitative assessment. Single cells from PBMCs, stem cells (iPSCs and H9 hESCs) and COs were seeded at a density of 200,000 cells per 100 μL FluoroBrite DMEM (Gibco) media per well in a 96-well black polystyrene plate (Greiner CELLSTAR, 655079). Single cells were evaluated based on two conditions: basal MMP (with JC-1 only) and inhibited MMP (100 μM FCCP + JC-1) as described above. Fluorescence readings from FCCP-treated and untreated samples were acquired using a Synergy H1 microplate reader (BioTek Instruments, Inc., 253147) and Gen5 Software with the following fluorescence excitation/emission settings: red J-aggregates (488 nm/595 nm) and green monomers (488 nm/535 nm). The ratio of fluorescence intensity of red to green is an indicator of the MMP. See Table S4 for biological and technical replicates.

ATP measurement. ATP levels were measured using CellTiter-Glo Luminescent Cell Viability Assay (Promega, G7570) according to manufacturer's instructions. Single cells from PBMCs, stem cells (iPSCs and H9 hESCs) and COs were seeded at a density of 50,000 cells per 100 μL culture media per well in a 96-well white polystyrene plate (Greiner CELLSTAR, 655083). An ATP standard curve was generated using ATP disodium salt (Sigma-Aldrich, A7699) ranging from 0 to 1 μM with 100 μL of 1 μM ATP solution containing 10^{-10} mol ATP. After addition of CellTiter-Glo Reagent (100 μL) to each well, contents were mixed on an orbital shaker for 2 min and luminescence readings from experimental samples and ATP standards were acquired using a Synergy H1 microplate reader (BioTek Instruments, Inc., 253147) and Gen5 Software. See Table S4 for biological and technical replicates.

Oligomycin treatment. To confirm whether the main source of ATP production is from OXPHOS or glycolysis in iPSCs and H9 hESCs, cells were first seeded at a density of 155,000 cells/cm^2 or 1.5 million cells/well in a clear 6-well plate format. Cells were visualized 24 h later to ensure proper attachment and health of the cells. Then, we treated the cells with 1 μM of Oligomycin for 30 min in MEF-conditioned media with a base DMEM/F12 that contains energy substrates, including high glucose and sodium pyruvate (Life Technologies, #11330057)[17]. The concentration and time of Oligomycin have been established in many Agilent Seahorse assays and and human pluripotent stem cell energy-profiling studies to inhibit OXPHOS-linked ATP production by blocking complex V, without inducing cell death in stem cells and cultured neurons[27,28,48]. Following treatment, cells were detached using Gentle Cell Dissociation Reagent (STEMCELL Technologies Inc) and propidium iodide staining on the Orflo Moxi Flow were used to assess cell count and viability. Cells were then seeded at a density of 50,000 cells per 100 μL culture media per well in a 96-well white polystyrene plate (155,000 cells/cm^2, Greiner CELLSTAR, 655083) and lysed immediately with CellTiter-Glo Reagent for endpoint ATP measurement as described above. As proof-of-concept, we treated whole H9 hESC COs (4 month) using Oligomycin and seeded the cells for endpoint ATP measurement as described above.

Luminex technology multiplex human oxidative phosphorylation (OXPHOS) magnetic bead panel. The assembly of mitochondrial complexes I to V in PBMCs, stem cells (H9 hESCs and iPSCs) and COs derived from H9 hESCs and iPSCs were measured using the Human Oxidative Phosphorylation Magnetic Bead Panel Milliplex MAP Kit (Millipore–H0XPSMAG-16K), following the manufacturer's instructions. Briefly, cell or tissue pellets were resuspended in Cell/Mitochondrial Lysis Buffer (as recommended by Millipore) with protease inhibitors (1:100, EMD Chemicals, Catalog #535140) and phosphatase inhibitors (1:50, EMD Chemicals, Catalog #524629). Protein lysates (500 μg/mL) were incubated with specific proprietary capture antibodies raised against the assembled OXPHOS protein complexes (I, II, III, IV and V) for 2 h at room temperature. The samples were then incubated with biotinylated secondary detection antibodies for 1 h at room temperature followed by incubation with streptavidin phycoerythrin conjugate for 30 min, which is the reporter molecule to complete the reaction. Samples were ran in five technical replicates. The intensity of the fluorescent signal was acquired using the Luminex Magpix system (Luminex Corporation xMAP Technology) and xPONENT software and analyzed using the MILLIPLEX Analyst 5.1 software. Results were expressed as normalized median fluorescence intensity. See Table S4 for biological and technical replicates.

Fluorescent immunohisto/cytochemistry for OXPHOS. Cerebral organoid cryosections (14 μm) thickness or cells (PBMCs, H9 hESCs and iPSCs) grown on glass coverslips were used for immunofluorescent staining. For tissues, samples were incubated in permeabilization/blocking solution (1X PBS pH 7.4, 10% Normal Donkey Serum, 2% BSA, 0.5% Triton X-100) for 1 h at room temperature in a humidified chamber. For cells, samples were permeabilized with 0.3% Triton X-100 (Sigma-Aldrich) in 1X PBS pH 7.4 for 15 min at room temperature and incubated in blocking solution (0.1% Tween-20 in 1X PBS pH 7.4, 1% BSA and 5% Normal Donkey Serum) for 1 h at room temperature. Proteins of interest were labeled with the following primary antibodies: NDUFS3 (mouse, abcam, ab110246, 1:100), SDHA (mouse, abcam, ab14715, 1:200), UQCRC1 (mouse, abcam, ab110252, 1:50), COXIV (mouse, abcam, ab33985, 1:200), ATP Synthase β (mouse, Invitrogen, A-21351,

1:500) and TOMM20 (rabbit, abcam, ab186734, 1:100) with specific combinations (NDUFS3 + TOMM20, SDHA + TOMM20, UQCRC1 + TOMM20, COXIV + TOMM20 and ATP Synthase β + TOMM20) diluted in antibody blocking solution (1X PBS pH 7.4, 0.1% Tween-20, 1% BSA, and 5% Normal Donkey Serum) and incubated overnight at 4 °C. Following overnight incubation, samples were washed three times (5 min per wash) with 0.1% Tween-20 in 1X PBS pH 7.4 and then incubated overnight at 4 °C (for tissues) or 1 h at room temperature (for cells) with the appropriate secondary antibodies: Donkey anti-Mouse IgG (H + L) Highly Cross-Adsorbed Secondary Antibody Alexa Fluor Plus 488 (Invitrogen, A23766) and Donkey anti-Rabbit IgG (H + L) Highly Cross-Adsorbed Secondary Antibody Alexa Fluor Plus 647 (Invitrogen, A32795) diluted 1:750 in antibody blocking solution. Following secondary antibody incubation, samples were washed three times in 1X PBS pH 7.4 with 0.1% Tween-20. Samples were counterstained with ProLong Gold Antifade Mountant with DAPI (Invitrogen) and left to cure overnight at room temperature protected from light. Images were captured using Leica TCS SP8 lightning confocal laser scanning microscope (DMI6000) equipped with white light laser (470–670 nm) and collected using LASX software (Lecia Microsystems). See Table S4 for biological and technical replicates.

Transmission electron microscopy. Mitochondrial number and morphology for PBMCs, stem cells (H9 hESCs and iPSCs) and COs derived from H9 hESCs and iPSCs were evaluated using Transmission Electron Microscopy. Samples (PBMCs, H9 hESCs, iPSCs, and COs) were fixed with primary fixation buffer (0.1 M phosphate buffer pH 7.2, 4% paraformaldehyde, 1% glutaraldehyde) for 2 h at room temperature and replaced with fresh fixative overnight at 4 °C. Following overnight incubation, samples (PBMCs, H9 hESCs, iPSCs, and COs) were washed three times for 20 min each with 0.1 M phosphate buffer at room temperature and underwent a secondary fixation with 1% osmium tetroxide in 0.1 M phosphate buffer for 1 h at room temperature in the dark. The samples (PBMCs, H9 hESCs, iPSCs, and COs) were again washed with 0.1 M phosphate buffer (pH 7.2) three times for 10 min each. Dehydration steps were performed on the samples by using a graded series of ethanol (EtOH) and distilled water at room temperature: 50% EtOH twice for 10 min each, 70% EtOH twice for 10 min each, 90% EtOH twice for 10 min each, and 100% EtOH three times for 15 min each. Once samples (PBMCs, H9 hESCs, iPSCs, and COs) were dehydrated, they were washed with a transitional solvent, propylene oxide, twice for 15 min each. The samples (PBMCs, H9 hESCs, iPSCs, and COs) were then infiltrated with epon resin using a graded series of epon and propylene oxide mixture at room temperature: (1) one part Epon resin mixed with two parts 100% propylene oxide for 1 h using an agitator; (2) two parts Epon resin mixed with one part 100% propylene oxide for 3 h using an agitator; (3) 100% epon overnight using an agitator and finally; (4) fresh 100% epon resin for 2 h. Once infiltration was complete, the samples (PBMCs, H9 hESCs, iPSCs, and COs) were placed in a Beem embedding capsule and polymerized at 60 °C for 48 h. After complete polymerization, the solid resin block containing the samples were sectioned on a Reichert Ultracut E microtome to 90 nm thickness and collected on 200 mesh copper grids. The sections were stained using saturated uranyl acetate for 15 min, rinsed in distilled water, followed by Reynold's lead citrate for 15 min and rinsed again in distilled water. The sections were examined and photographed using a FEI Talos L120C transmission electron microscope at an accelerating voltage of 80 kV.

References

1. Spinelli, J. B. & Haigis, M. C. The multifaceted contributions of mitochondria to cellular metabolism. *Nat. Cell Biol.* **20**(7), 745–754. https://doi.org/10.1038/s41556-018-0124-1 (2018).
2. Nunnari, J. & Suomalainen, A. Mitochondria: In sickness and in health. *Cell* **148**(6), 1145–1159. https://doi.org/10.1016/j.cell.2012.02.035 (2012).
3. Picard, M. & McEwen, B. S. Mitochondria impact brain function and cognition. *Proc. Natl. Acad. Sci. USA.* **111**(1), 7–8. https://doi.org/10.1073/pnas.1321881111 (2014).
4. Herculano-Houzel, S. The remarkable, yet not extraordinary, human brain as a scaled-up primate brain and its associated cost. *Proc. Natl. Acad. Sci. USA.* **109**(Suppl 1), 10661–10668. https://doi.org/10.1073/pnas.1201895109 (2012).
5. Bélanger, M., Allaman, I. & Magistretti, P. J. Brain energy metabolism: Focus on astrocyte-neuron metabolic cooperation. *Cell Metab.* **14**(6), 724–738. https://doi.org/10.1016/j.cmet.2011.08.016 (2011).
6. Sharpley, M. S. *et al.* Heteroplasmy of mouse mtDNA is genetically unstable and results in altered behavior and cognition. *Cell* **151**(2), 333–343. https://doi.org/10.1016/j.cell.2012.09.004 (2012).
7. Hara, Y. *et al.* Presynaptic mitochondrial morphology in monkey prefrontal cortex correlates with working memory and is improved with estrogen treatment. *Proc. Natl. Acad. Sci. USA.* **111**(1), 486–491. https://doi.org/10.1073/pnas.1311310110 (2014).
8. Consortium P. Revealing the brain's molecular architecture. *Science* **362**(6420), 1262–1263. https://doi.org/10.1126/science.362.6420.1262 (2018).
9. Akbarian, S. *et al.* The PsychENCODE project. *Nat. Neurosci.* **18**(12), 1707–1712. https://doi.org/10.1038/nn.4156 (2015).
10. Lancaster, M. A. & Knoblich, J. A. Generation of cerebral organoids from human pluripotent stem cells. *Nat. Protoc.* **9**(10), 2329–2340. https://doi.org/10.1038/nprot.2014.158 (2014).
11. Lancaster, M. A. *et al.* Cerebral organoids model human brain development and microcephaly. *Nature* **501**(7467), 373–379. https://doi.org/10.1038/nature12517 (2013).
12. Mariani, J. *et al.* FOXG1-dependent dysregulation of GABA/glutamate neuron differentiation in autism spectrum disorders. *Cell* **162**(2), 375–390. https://doi.org/10.1016/j.cell.2015.06.034 (2015).
13. Bershteyn, M. *et al.* Human iPSC-derived cerebral organoids model cellular features of lissencephaly and reveal prolonged mitosis of outer radial glia. *Cell Stem Cell* **20**(4), 435–449.e4. https://doi.org/10.1016/j.stem.2016.12.007 (2017).
14. Weinstein, G. D. & Van Scott, E. J. Autoradiographic analysis of turnover times of normal and psoriatic epidermis. *J. Investig. Dermatol.* **45**(4), 257–262 (1965).

15. Gattinoni, L. *et al.* A human memory T cell subset with stem cell-like properties. *Nat. Med.* **17**(10), 1290–1297. https://doi.org/10.1038/nm.2446 (2011).
16. Okita, K. *et al.* An efficient nonviral method to generate integration-free human-induced pluripotent stem cells from cord blood and peripheral blood cells. *Stem Cells.* **31**(3), 458–466. https://doi.org/10.1002/stem.1293 (2013).
17. Sivitilli, A. A. *et al.* Robust production of uniform human cerebral organoids from pluripotent stem cells. *Life Sci. Alliance.* https://doi.org/10.26508/lsa.202000707 (2020).
18. Taylor, R. W. & Turnbull, D. M. Mitochondrial DNA mutations in human disease. *Nat. Rev. Genet.* **6**(5), 389–402. https://doi.org/10.1038/nrg1606 (2005).
19. Hämäläinen, R. H. Mitochondrial DNA mutations in iPS cells: mtDNA integrity as standard iPSC selection criteria?. *EMBO J.* **35**(18), 1960–1962. https://doi.org/10.15252/embj.201695185 (2016).
20. Druzhyna, N. M., Wilson, G. L. & LeDoux, S. P. Mitochondrial DNA repair in aging and disease. *Mech. Ageing Dev.* **129**(7–8), 383–390. https://doi.org/10.1016/j.mad.2008.03.002 (2008).
21. Kang, E. *et al.* Age-related accumulation of somatic mitochondrial DNA mutations in adult-derived human iPSCs. *Cell Stem Cell* **18**(5), 625–636. https://doi.org/10.1016/j.stem.2016.02.005 (2016).
22. Hussein, S. M. *et al.* Copy number variation and selection during reprogramming to pluripotency. *Nature* **471**(7336), 58–62. https://doi.org/10.1038/nature09871 (2011).
23. Folmes, C. D. *et al.* Disease-causing mitochondrial heteroplasmy segregated within induced pluripotent stem cell clones derived from a patient with MELAS. *Stem Cells.* **31**(7), 1298–1308. https://doi.org/10.1002/stem.1389 (2013).
24. Perelman, A. *et al.* JC-1: Alternative excitation wavelengths facilitate mitochondrial membrane potential cytometry. *Cell Death Dis.* **3**, e430. https://doi.org/10.1038/cddis.2012.171 (2012).
25. Mathur, A., Hong, Y., Kemp, B. K., Barrientos, A. A. & Erusalimsky, J. D. Evaluation of fluorescent dyes for the detection of mitochondrial membrane potential changes in cultured cardiomyocytes. *Cardiovasc. Res.* **46**(1), 126–138. https://doi.org/10.1016/s0008-6363(00)00002-x (2000).
26. Xu, X. *et al.* Mitochondrial regulation in pluripotent stem cells. *Cell Metab.* **18**(3), 325–332. https://doi.org/10.1016/j.cmet.2013.06.005 (2013).
27. Zhang, J. *et al.* Measuring energy metabolism in cultured cells, including human pluripotent stem cells and differentiated cells. *Nat. Protoc.* **7**(6), 1068–1085. https://doi.org/10.1038/nprot.2012.048 (2012).
28. Khacho, M. *et al.* Mitochondrial dynamics impacts stem cell identity and fate decisions by regulating a nuclear transcriptional program. *Cell Stem Cell* **19**(2), 232–247. https://doi.org/10.1016/j.stem.2016.04.015 (2016).
29. Folmes, C. D. *et al.* Somatic oxidative bioenergetics transitions into pluripotency-dependent glycolysis to facilitate nuclear reprogramming. *Cell Metab.* **14**(2), 264–271. https://doi.org/10.1016/j.cmet.2011.06.011 (2011).
30. Bean, B. P. The action potential in mammalian central neurons. *Nat. Rev. Neurosci.* **8**(6), 451–465. https://doi.org/10.1038/nrn2148 (2007).
31. Luo, C. *et al.* Cerebral organoids recapitulate epigenomic signatures of the human fetal brain. *Cell Rep.* **17**(12), 3369–3384. https://doi.org/10.1016/j.celrep.2016.12.001 (2016).
32. Nascimento, J. M. *et al.* Human cerebral organoids and fetal brain tissue share proteomic similarities. *Front. Cell Dev. Biol.* **7**, 303. https://doi.org/10.3389/fcell.2019.00303 (2019).
33. Camp, J. G. *et al.* Human cerebral organoids recapitulate gene expression programs of fetal neocortex development. *Proc. Natl. Acad. Sci. USA.* **112**(51), 15672–15677. https://doi.org/10.1073/pnas.1520760112 (2015).
34. Tanaka, Y., Cakir, B., Xiang, Y., Sullivan, G. J. & Park, I. H. Synthetic analyses of single-cell transcriptomes from multiple brain organoids and fetal brain. *Cell Rep.* **30**(6), 1682–1689.e3. https://doi.org/10.1016/j.celrep.2020.01.038 (2020).
35. Giandomenico, S. L. & Lancaster, M. A. Probing human brain evolution and development in organoids. *Curr. Opin. Cell Biol.* **02**(44), 36–43. https://doi.org/10.1016/j.ceb.2017.01.001 (2017).
36. Gyllensten, L. Oxygen exposure and brain damage. *Nature* **183**(4667), 1068–1069. https://doi.org/10.1038/1831068a0 (1959).
37. Wimmer, R. A. *et al.* Human blood vessel organoids as a model of diabetic vasculopathy. *Nature* **565**(7740), 505–510. https://doi.org/10.1038/s41586-018-0858-8 (2019).
38. Mansour, A. A. *et al.* An in vivo model of functional and vascularized human brain organoids. *Nat. Biotechnol.* **36**(5), 432–441. https://doi.org/10.1038/nbt.4127 (2018).
39. Ao, Z. *et al.* One-stop microfluidic assembly of human brain organoids to model prenatal cannabis exposure. *Anal. Chem.* **92**(6), 4630–4638. https://doi.org/10.1021/acs.analchem.0c00205 (2020).
40. Andreazza, A. C. *et al.* Guidelines for the standardized collection of blood-based biomarkers in psychiatry: Steps for laboratory validity—a consensus of the Biomarkers Task Force from the WFSBP. *World J. Biol. Psychiatry.* https://doi.org/10.1080/15622975.2019.1574024 (2019).
41. Martí, M. *et al.* Characterization of pluripotent stem cells. *Nat. Protoc.* **8**(2), 223–253. https://doi.org/10.1038/nprot.2012.154 (2013).
42. Picard, M. *et al.* Mitochondrial functions modulate neuroendocrine, metabolic, inflammatory, and transcriptional responses to acute psychological stress. *Proc. Natl. Acad. Sci. USA.* **112**(48), E6614–E6623. https://doi.org/10.1073/pnas.1515733112 (2015).
43. Liang, K. X. *et al.* Disease-specific phenotypes in iPSC-derived neural stem cells with POLG mutations. *EMBO Mol. Med.* https://doi.org/10.15252/emmm.202012146 (2020).
44. Martin, S. A. *et al.* GSK3β regulates brain energy metabolism. *Cell Rep.* **23**(7), 1922–1931.e4. https://doi.org/10.1016/j.celrep.2018.04.045 (2018).
45. Roy-Choudhury, G. & Daadi, M. M. Assay for assessing mitochondrial function in iPSC-derived neural stem cells and dopaminergic neurons. *Methods Mol. Biol.* **1919**, 161–173. https://doi.org/10.1007/978-1-4939-9007-8_12 (2019).
46. Gautier, I., Geeraert, V., Coppey, J., Coppey-Moisan, M. & Durieux, C. A moderate but not total decrease of mitochondrial membrane potential triggers apoptosis in neuron-like cells. *NeuroReport* **11**(13), 2953–2956. https://doi.org/10.1097/00001756-200009110-00024 (2000).
47. Kitayama, H. *et al.* Human immunodeficiency virus type 1 Vpr inhibits axonal outgrowth through induction of mitochondrial dysfunction. *J. Virol.* **82**(5), 2528–2542. https://doi.org/10.1128/JVI.02094-07 (2008).
48. Chen, H., Tian, J., Guo, L. & Du, H. Caspase inhibition rescues F1Fo ATP synthase dysfunction-mediated dendritic spine elimination. *Sci. Rep.* **10**(1), 17589. https://doi.org/10.1038/s41598-020-74613-9 (2020).

Acknowledgements

Author contributions

Funding

Competing interests

The authors declare no competing interests.

Additional information

Supplementary Information The online version contains supplementary material available at https://doi. org/10.1038/s41598-021-84071-6.

Correspondence and requests for materials should be addressed to J.-M.B., L.A. or A.C.A.

Reprints and permissions information is available at www.nature.com/reprints.

Publisher's note Springer Nature remains neutral with regard to jurisdictional claims in published maps and institutional affiliations.